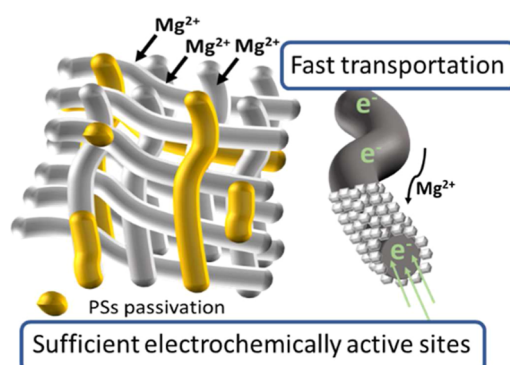# Insights into the Degradation Mechanism of the Magnesium Anode in Magnesium−Chalcogen Batteries: Revealing Principles for Anode Design with a 3D-Structured Magnesium Anode

Liping Wang,* Thomas Diemant, Zhenyou Li, Bosubabu Dasari, and Zhirong Zhao-Karger*

ABSTRACT: Magnesium−chalcogen batteries are promising post lithium battery systems for large-scale energy storage applications in terms of energy density, material sustainability, safety, and cost. However, the soluble reaction intermediates, such as polysulfides or polyselenides, formed during the electrochemical processes can severely passivate the Mg metal anode, limiting the cycle life of the batteries. It is necessary to rescrutinize the failure in Mg−chalcogen batteries from an anodic perspective. Herein, the Mg metal anode failure mechanism is thoroughly examined, revealing that it is induced by an inhomogeneous Mg deposition promoted by soluble intermediates from chalcogen cathodes. To further confirm the mechanism and solve this anode failure problem, a multifunctional 3D current collector is used to decrease the local current density and regulate the Mg deposition behavior. The present findings are anticipated to provide guidance for anode design, enhance the life-span of Mg−chalcogen batteries, and facilitate the development of other magnesium metal batteries.

KEYWORDS: 3D magnesium anode, inhomogeneous Mg deposition, anode passivation, polysulfideshuttle, magnesium−chalcogen batteries

1. INTRODUCTION

Rechargeable magnesium batteries (RMBs) have shown great potential as a cost-effective, safe, and environmentally friendly technology for electrochemical energy storage and conversion. Magnesium metal has a low reduction potential [−2.36 V vs standard hydrogen electrode] and high theoretical capacities ($3832 \, mA \, h \, cm^{-3}$, $2205 \, mA \, h \, g^{-1}$). The natural abundance of Mg was determined to be the eighth and the third in Earth's crust and sea water, respectively, indicating promising availability and low cost for large-scale applications. Besides, in contrast to lithium, magnesium is less susceptible to dendrite formation during deposition and may be a good choice for a safe metal anode.[1−7] When coupled with a sustainable chalcogen cathode, such as sulfur (S) or selenium (Se), Mg−chalcogen batteries possess a higher theoretical volumetric capacity than Li−chalcogen batteries, making them a promising candidate for emerging energy storage markets.[8−10]

In comparison with the progress made in the fields of electrolytes and cathodes, there has been less research work concentrated on the Mg anode. The Mg metal foil is considered to be used both as an electrode and a current collector, which is thought advantageous for a battery system. Though this concept is attractive, there are still formidable challenges in practice. First, magnesium offers slower reaction kinetics compared to lithium due to the divalent magnesium ion with higher charge density ($120 \, C \, mm^{-3}$ for Mg^{2+} vs $52 \, C \, mm^{-3}$ for Li^+).[11,12]

Second, with a hexagonal structure, Mg has a limited ductility, making it difficult to cost-effectively form the desired thin foil as an anode for RMBs.[13,14] Additionally, the unavoidable interactions between Mg metal and organic electrolyte solutions have been found to play a crucial role in the electrochemical performance of RMBs.[15,16] It is well known that lithium-ion batteries are able to form solid electrolyte interfaces via reactions with the electrolyte, which allow the transport of lithium ions between the anode and the electrolyte without substantial degradation.[17] In contrast, magnesium strongly tends to form insulating passivation layers[18−21] or surface adlayers composed of some species in the electrolyte. The coverage layers on the Mg surface may increase interfacial resistance and kinetic barriers for Mg^{2+} transfer, leading to high overpotential and low Coulombic efficiency for Mg plating and stripping.[22] The problem is getting even worse when using chalcogen cathodes, such as in Mg−S and Mg−Se batteries. After the dissolution of magnesium polysulfides/polyselenides (Mg-PSs) into the electrolyte, they
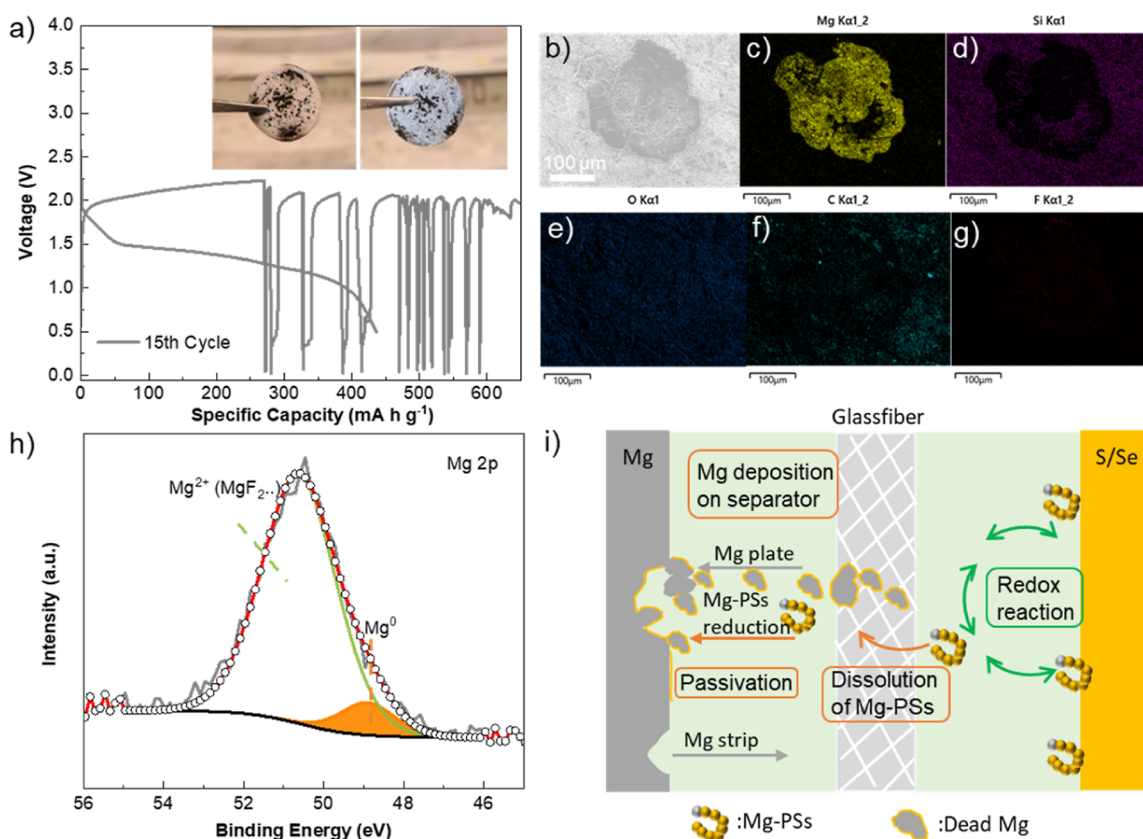
Figure 1. (a) Galvanostatic discharge/charge curve of a Mg−S cell when it failed (inset shows the photographs of the Mg anode (right) and glass fiber separator (left) obtained from this cell after disassembly). (b) SEM image, (c−g) EDX maps, and (h) Mg 2p XPS spectrum of a glass fiber separator after disassembling from a Mg−S cell and washing with the DME solvent. (i) Schematic depiction of the failure mechanism of Mg metal anodes in Mg− S batteries.

may diffuse across the separator to the Mg anode, where they can be further reduced, leading to the acceleration of detrimental passivation on the Mg anode. As a result, Mg−S/Mg−Se systems have mostly reported short cycle lives, especially without a Li mediator or corrosive halogen compounds inside the electrolyte.[23−30] There are some pioneering works about electrolyte engineering[31,32] and cathode modification.[33] However, to the best of our knowledge, there is a lack of studies on the dynamic evolution of the Mg metal anode during cycling and its correlation with the degradation or failure of Mg−S/Mg−Se batteries.

Various cathode and separator design strategies have been proposed in order to control the dissolution and diffusion of polysulfide from the cathode to the anode side in Mg−S/Mg−Se batteries.[34−36] In contrast, less research effort was devoted to the optimization of anode materials for Mg−chalcogen batteries. Sievert et al. dispersed fine Mg particles in carbon and demonstrated the effectiveness of structure design for the improvement of Mg−S batteries. However, finely dispersed magnesium may strongly react with oxygen in air, and passivation may occur when handling the material.[37] In fact, the composition and morphology of the electrolyte/anode interface may considerably affect the electrochemical performance of the batteries.[38,39] To tackle the critical issues in Mg−chalcogen batteries, it is also required to design the structure of the magnesium anode rationally.

Herein, a systematic investigation was carried out to discover the underlying reasons for the Mg−S and Mg−Se batteries' failure. To further confirm the mechanism and circumvent the

obstacles originating from the Mg foil anode, a novel structure of the Mg anode based on a multifunctional 3D current collector was designed. A freestanding active carbon cloth (ACC) acts as the 3D current collector, which provides two advantages: (1) the enlarged surface area of the ACC lowers the local current density, which enables uniform magnesium electrochemical deposition; (2) the interconnected scaffold of the ACC can improve the contact between electrolyte and electrode, fasten Mg^{2+} ion transport, and improve the kinetics of the electrode. Remarkably, these ACC-based anodes can greatly alleviate the early failure of Mg−S/Mg−Se cells. This study highlights the metal anode degradation mechanism in Mg−S/Mg−Se batteries and provides guidelines for a reasonable structural design of metal anodes in magnesium-based batteries.

2. RESULTS AND DISCUSSION

2.1. Failure Mechanism of the Magnesium Anode in Mg−S Batteries. Coin cells comprised of a 0.4 M Mg[B-(hfip)$_4$]$_2$ electrolyte,[40] an activated carbon cloth/sulfur (ACC/S) cathode, and a Mg foil anode were cycled at a current rate of 0.1 C. To reveal the origin of high polarization and fast degradation of Mg−S cells composed of a Mg foil anode and a ACC/S cathode, we first conducted scanning electron microscopy (SEM)−energy dispersive X-ray spectroscopy (EDX) and X-ray photoelectron spectroscopy (XPS) analysis of the Mg foil anode and separator (close to the anode side) by recovering the coin cells after failure (Figure 1). The typical discharge/charge curve when a cell fails is shown in Figure 1a. The failure always occurred during the charge process showing a
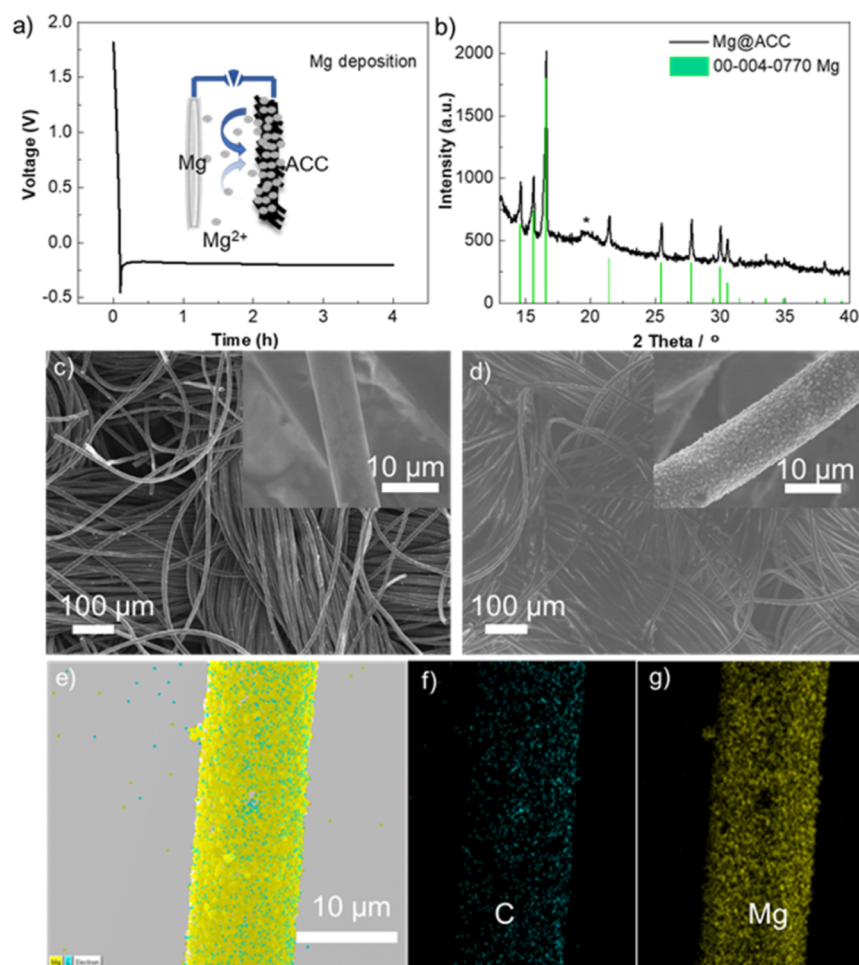
Figure 2. (a) Mg plating profile of a Mg|ACC cell (inset: schematic illustration of Mg deposition on ACC). (b) XRD pattern of Mg@ACC. (c,d) Typical SEM images of (c) ACC and (d) Mg@ACC (Mg: 4 mA h cm^{-2}). (e–g) EDX maps of Mg@ACC.

fluctuating curve, which could not reach the upper cutoff voltage anymore. This phenomenon was also observed and reported before.[9,35,36,41] The photographs in the inset of Figure 1a illustrate the Mg foil and the separator disassembled from the failing cell. Some black spots could be clearly observed on both the anode and separator, where the electrochemical reactions took place. The following analyses were carried out mainly on these black spots. Figures S1−S3 demonstrate the morphology and elemental distribution of the Mg anode (Figures S1 and S2) and separator (Figure S3) without further treatment. As can be seen, the Mg surface was rugged accompanied by caves and pits, which resulted from the Mg stripping process. On the pits, there are many porous, irregularly deposited Mg particles, indicating the nonuniform Mg plating. Furthermore, EDX mapping shows a more intense sulfur signal for the deposits on both anode and separator than for the rest areas, indicating that deposits are more susceptible to form sulfur-containing byproducts or passivation layers than the bulk Mg (Mg substrate). Similar to the separator, the EDX spectrum (Figure S3) indicates that these black deposits are mainly composed of Mg, with some sulfur (S), oxygen (O), carbon (C), and fluorine (F). To further figure out the composition of the black deposits, the separator was rinsed with dimethoxy ethane (DME) in a glovebox to remove the residual electrolyte salt and soluble Mg-PSs (Figure S4). After washing, there were still lots of black spots on the separator, and the color of the DME solvent turned red−brown

(Figure S4b), indicating dissolved Mg-PSs. The top surface and cross-sectional SEM images of the washed separators in Figure S5 illustrate similar structures of these deposits as micrometer-sized islands. The ones circled in red (Figure S5d−f) were observed from cross-sectional SEM images, indicating the penetration of the deposits through the separator. The corresponding cross-sectional EDX maps of the separator are displayed in Figure S6. The distribution of Mg element confirms that the deposits were distributed not only on the surface but also through the separator. In order to elaborate on the composition, the deposits on the DME washed separator were analyzed by XPS. The Mg 2p spectrum (Figure 1h) could be fitted with two peaks at 48.9 and 50.6 eV, which are assigned to metallic Mg^0 and various Mg^{2+}-containing compounds, for example, MgF$_2$. The results confirm that the black spots on the separator are composed of a freshly deposited Mg core with some byproducts from parasitic reactions on the surface. The corresponding F 1s spectrum (Figure S7a) showed two peaks at 685.5 and 688.6 eV, corresponding to MgF$_2$ and −CF$_3$ groups (from the remaining electrolyte), respectively. The O 1s spectrum (Figure S7b) could be fitted with three peaks at 532.7 eV (SiO$_2$/separator), 531.8 eV (C=O), and 533.3 eV (C−O), which originated from a short period of air-exposure during the ex situ measurements and residuals of the DME solvent used for washing the separator. Interestingly, sulfur was not detectable in the measurements, most probably any S species
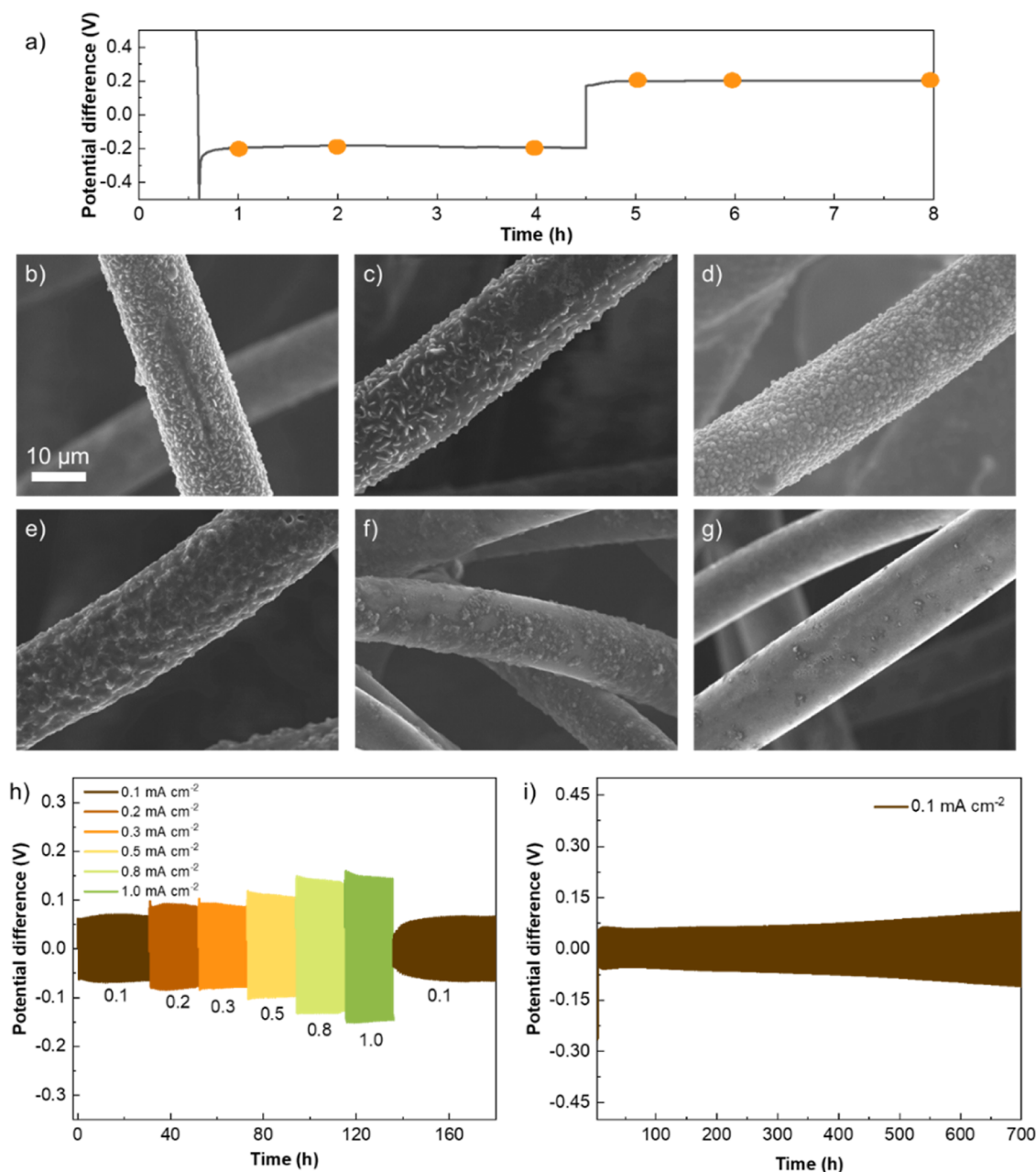
Figure 3. (a) Illustration of the discharge/charge process of the Mg@ACC electrode. Typical SEM images of Mg@ACC after plating Mg metal into ACC for (b) 1, (c) 2, and (d) 4 h and then stripping Mg for (e) 1, (f) 2, and (g) 4 h from Mg@ACC. (h) Mg plating/stripping performance of the Mg|Mg@ACC cell at various current densities (from 0.1 to 1.0 mA cm^{-2}) for a plating/stripping time of 0.5 h. (i) Long-term cycling of the Mg|Mg@ACC cell at 0.1 mA cm^{-2}.

were removed by washing or evaporated in the load lock of the XPS system before the measurement. A direct comparison of the different compositions of the black spots and the rest area of the separator is shown in Figure S8. As expected, the ratio of Mg is much higher in the deposits than in the rest areas, which corresponds to the XPS results.

Taken together, it is rational to postulate that the failure of Mg anodes is highly related to the inhomogeneous nucleation and growth of Mg on the metal foil due to the unavoidable inhomogeneity of the metal electrode surface.[42−46] In addition, dissolved polysulfide species further accelerate this uneven deposition in Mg−S batteries. As illustrated in Figure 1i, fresh Mg starts to deposit during the charge process. Simultaneously, the dissolved polysulfides accumulate on the surface of the fresh

Mg and may subsequently passivate the Mg or be further reduced by the fresh Mg,[47] forming Mg-PSs wrapped "dead Mg". Similar phenomena were reported in batteries with a lithium-metal anode.[48−51] The high ionic resistance of the polysulfide passivation layer downsizes the nuclei and thus results in a more uneven Mg deposition. This situation severely deteriorates with cycles, where more and more brittle Mg deposits accumulate around the cavities. They are easy to detach from the Mg foil, inducing aggravated local etching and the formation of isolated "dead Mg". Some of them travel with the electrolyte and penetrates the separator, leading to the failure of the cell. This also explains the phenomenon that the failure always occurrs during the charge process, and the fluctuating shape of the charge curve may relate to the unstable "dead Mg".
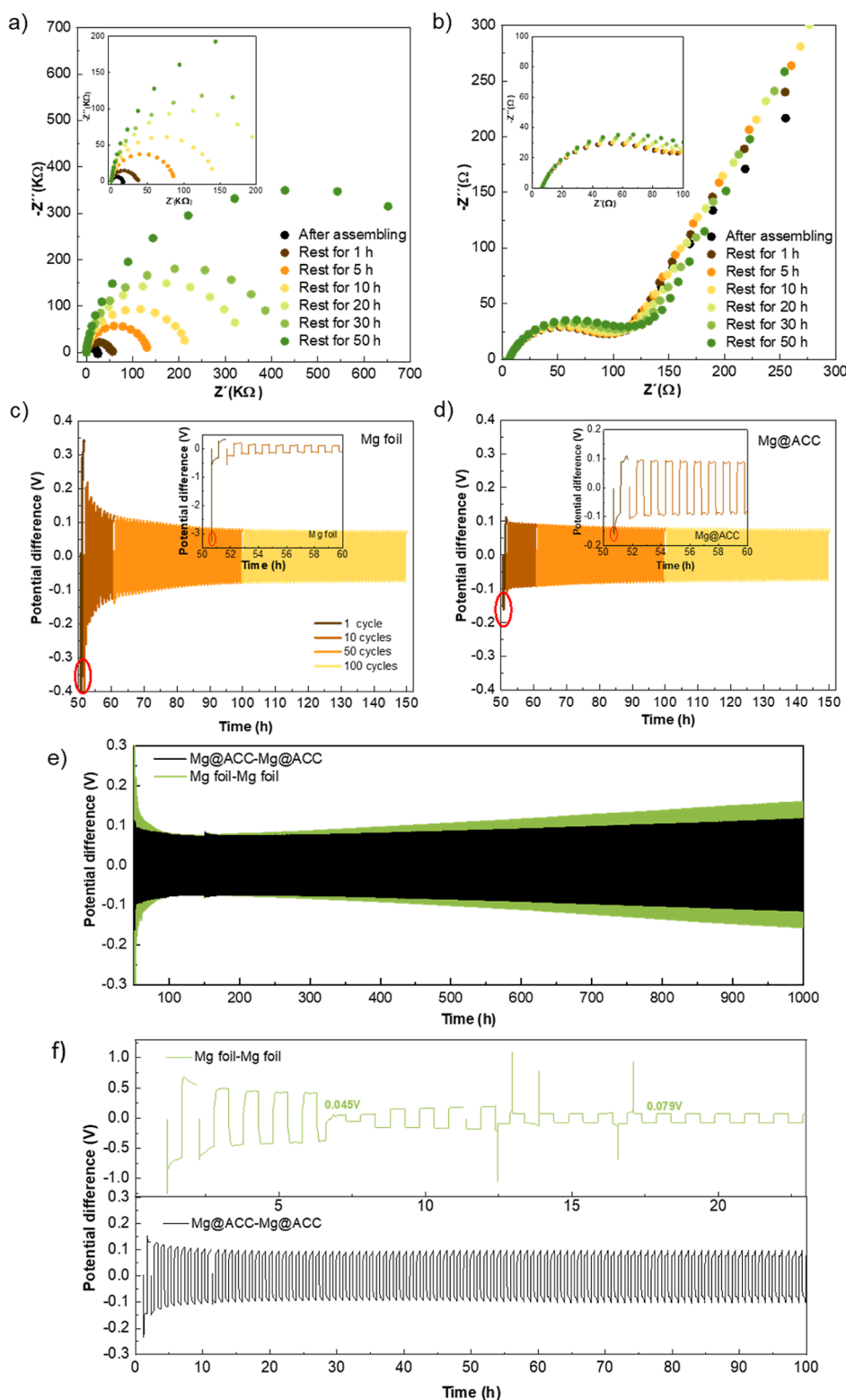
Figure 4. Nyquist plots of (a) Mg foil|Mg foil and (b) Mg@ACC|Mg@ACC cells in the frequency range of 1 MHz to 20 mHz with different rest times at OCV. Mg plating/stripping performance of symmetric (c) Mg foil|Mg foil and (d) Mg@ACC|Mg@ACC cells at the current density of 0.1 mA cm^{-2}. Insets: enlarged profiles of the first 10 cycles. Galvanostatic plating/stripping profiles in Mg@ACC|Mg@ACC and Mg|Mg symmetrical cells at 0.1 mA cm^{-2} with (e) blank electrolyte and (f) electrolyte dissolved with polysulfides.

Based on the abovementioned results and analysis, we conclude that it is necessary to find a way to allow a uniform Mg deposition in order to ensure the performance of the Mg anode for Mg−S/Mg−Se batteries. Many researchers have reported that 3D current collectors can provide large surface areas, thus decreasing the local current density and regulating the Li metal deposition.[52,53] Inspired by their works, ACC has been employed as a multifunctional 3D current collector for the

Figure 5. Comparison of the electrochemical performance of Mg–S cells with Mg@ACC and a Mg foil anode in coin cell or three-electrode cell setups. Coin cell: (a) charge−discharge profile of the first cycle; (b) cyclic voltammetry curves. Three-electrode cell: (c) cyclic voltammetry curves; (d) potentials of the counter electrode (E_{CE}) versus reference electrode (E_{RE}). Schematic illustrations of (e) Mg@ACC and (f) Mg foil anodes during the Mg-plating process in Mg–S cells.

Mg anode (noted as Mg@ACC) to comprehensively examine the influences of Mg electrodeposition on the performance, especially for Mg–S or Mg–Se systems.

2.2. Morphology and Electrochemical Performance of Mg@ACC. Figure 2a illustrates schematically the electrodeposition process and the corresponding voltage curve for preparing the Mg@ACC anode. The electrodeposition was conducted by applying a constant current density of 1 mA cm^{-2} for 4 h. From the voltage profile, stable magnesium electrodeposition was achieved in 0.4 M Mg[B(hfip)$_4$]$_2$ electrolyte at a voltage of around −0.2 V versus Mg^{2+}/Mg. As shown in Figure 2b, the X-ray diffraction (XRD) pattern of the Mg@ACC is well-indexed to hexagonally close packed magnesium. Besides, the weak reflection at around 19.5° is corresponding to the carbon cloth. To reveal the morphological changes before and after magnesium deposition, the electrodes were observed with SEM; the images are displayed in Figure 2c,d. For the pristine ACC,

the surface of the carbon fiber was quite smooth (Figure 2c). After electrodeposition, magnesium metal was accommodated in the ACC matrix alongside the fibers in a rather compact way, displaying a uniform topography (Figure 2d). The corresponding EDX maps and spectrum of the Mg@ACC are displayed in Figures 2e−g and S9. The EDX results exhibit strong Mg signals across the ACC network; the other elements (C, O, and F) come from the residual electrolyte and the carbon fiber. These results confirm that magnesium can be deposited on ACC compactly without introducing other impure phases.

The magnesium metal stripping/plating behavior on the ACC was investigated in more detail by collecting SEM images at different states of the discharging/charging process (Figure 3a). Initially, the carbon fibers were surrounded by Mg^{2+} after resting for 1 h. As the voltage decreased below 0 V, the nucleated Mg metal started to grow on the conductive carbon fibers (Figure 3b). With extended plating times (2 and 4 h), a homogeneous

magnesium metal layer gradually grew on the carbon fibers (Figure 3c,d). Upon stripping, magnesium was oxidized again and started to lose electrons and dissolve back into the electrolyte (Figure 3e,f). After being fully charged, the framework of the ACC remained intact (Figure 3g), suggesting its good structural stability. Taken together, these results show that the plating/stripping process of magnesium on the ACC is highly reversible, which guarantees the stable cycling performance of the electrode. To demonstrate the electrochemical behavior of a Mg@ACC electrode, symmetric Mg|Mg@ACC cells were tested at various current densities. As shown in Figure 3h, the overpotentials increased slightly with growing current densities and became stable within a few cycles. Even at the relatively high current density of 1.0 mA cm^{-2}, the cell maintained a low polarization of about 0.12 V. A long-term cyclability test with a current of 0.1 mA cm^{-2} is displayed in Figure 3i. The cell allowed stable operation for more than 700 cycles while maintaining a low polarization below 0.15 V. Long-term cycling performance at a higher current density of 0.5 mA cm^{-2} was also investigated; the results are presented in Figure S10. The cell still shows excellent cyclic stability with an overpotential below 0.15 V after 400 cycles. All these results demonstrate that highly reversible plating/stripping of Mg can be realized successfully with small overpotentials by using a Mg@ACC electrode.

To gain more information about the differences in the electrode/electrolyte interfaces between the Mg foil anode and Mg@ACC, electrochemical impedance spectra (EIS) were acquired for symmetric Mg foil|Mg foil and Mg@ACC|Mg@ACC cells after various rest times at open-circuit voltage (OCV). Figure 4a displays the Nyquist plots measured with a Mg foil|Mg foil symmetric cell. The impedance was measured to be 24 kΩ after assembly and kept increasing incrementally with the rest time. After 50 h, the resistance reached 787 kΩ (i.e., more than 30 times the initial value). This result is in agreement with the previous literatures.[15,40] The increasing resistance of the Mg electrode may be related to the formation of an adsorption layer from the solvent, which accounts for the difference in the initial voltage spike (−3.24 V) in Figure 4c. For the Mg@ACC|Mg@ACC cell, the impedance was observed to stabilize at approximately 100 Ω with various storage times at OCV (Figure 4b), roughly three orders of magnitude lower than for the Mg foil|Mg foil cell. Correspondingly, the initial voltage spike with Mg@ACC was much reduced to −0.16 V, as shown in Figure 4d. Both the low interfacial resistance and small initial voltage spike point to fast charge transfer on the interface of a Mg@ACC electrode. The galvanostatic intermittent titration technique was also used to further confirm the low polarization of the cell with Mg@ACC, as shown in Figure S11. Besides, the long-term cycling stability of symmetric cells was further tested (Figure 4e, enlarged profiles shown in Figure S12). Compared with bare Mg foil (green), the Mg@ACC (black) symmetric cells displayed a lower voltage polarization and improved plating/stripping stability up to 1000 cycles, revealing the excellent reversible Mg stripping/plating behavior. To evaluate the performance of the two kinds of the Mg electrode with the dissolved magnesium polysulfide, an additional 40 μL magnesium polysulfide solution was added inside the cells. The polysulfide solution (Figure S13) was prepared according to a reported procedure.[40] With the polysulfide-containing electrolyte (Figure 4f), the cell with the Mg foil anode (green) shows a high overpotential at the beginning and decreases significantly to 0.045 V after 7 h. After that, the voltage curve displays a rectangular shape, which

corresponds to a soft short-circuit behavior.[44] While the cell with Mg@ACC (black) displays a stable stripping/plating with a voltage hysteresis around 0.09 V after 100 cycles, which demonstrates the high tolerance to polysulfides.

2.3. Electrochemical Performances of Mg−Chalcogen Batteries.
In the next step, the performance of Mg@ACC anodes in Mg−S batteries was investigated using a model ACC/S composite as a cathode material. The ACC/S cathode was fabricated via a commonly used melt-diffusion method, as reported before.[10] The SEM and EDX images of ACC/S in Figure S14 demonstrate the uniform dispersion of sulfur in the porous carbon fibers. Both Mg@ACC and Mg foil anodes were paired with the ACC/S cathode and assembled in coin cells. In comparison to the cell with Mg foil, the Mg@ACC cell showed a lower voltage hysteresis in the first cycle charge−discharge profiles and cyclic voltammetry curves, as shown in Figure 5a,b. The voltage hysteresis can be roughly analyzed by the galvanostatic charge−discharge curves shown in Figure S15. Apart from that, three-electrode cells were also assembled with ACC/S as the working electrode, Mg foil or Mg@ACC as counter electrode (CE), and a Mg ring as reference electrode (RE), respectively. As shown in Figure 5c, considering the working electrode, the main reduction peak of the cell with a Mg@ACC anode emerged at around 1.44 V during the first cathodic scan, while the oxidation peak appeared at around 1.92 V with respect to the Mg_{RE} electrodes. With Mg foil as anode, both the cathodic and anodic signal shifted towards higher voltage polarization (1.31 and 2.03 V, respectively). In parallel, the corresponding voltage versus E_{CE} were recorded, showing an obvious difference between the two cells with different anodes. The reduction peaks overlapped for the cell with the Mg@ACC anode, suggesting a negligible overpotential during the Mg stripping process with Mg@ACC. In contrast, with the bare Mg anode, a detectable overpotential of 0.119 V was noted during discharge. The potential differences were more apparent during cathode oxidation/anode reduction, which is attributed to the higher energy barrier for Mg plating, resulting from the competition between the reduction of sulfur species and Mg^{2+}.[26,54] The overpotential of the Mg@ACC anode during the charge process was around 0.15 V lower than for the bare Mg anode. The results can be further confirmed by the voltage profiles of counter electrode (E_{CE}) versus reference electrode (E_{RE}), which are presented in Figure 5d. Similarly, the voltage hysteresis during Mg plating is more prominent compared to Mg stripping and the voltage polarization of the Mg@ACC anode is much lower than that of the Mg foil anode. The decreased voltage hysteresis of the Mg@ACC anode coincides with the reduced current density stemming from the high surface area of the carbon framework with extended electrochemically active sites and less insulating passivation.

To monitor the differences in the interfacial conditions, the anode impedance of three-electrode cells with the Mg anode and the Mg@ACC anode was recorded (Figure S16). Similar to prior studies,[35] a large resistance of around 4500 Ω was recorded in a fresh cell with a Mg foil anode, which increased vastly to about 6000 Ω after 1 h of rest. For the Mg@ACC anode, an impressive decrease of the resistance to 200 Ω was observed after assembly, and it remained stable after 1 h of rest. It is plausible that the different interfacial resistances are responsible for the different stripping behaviors with the different initial voltage spikes mentioned before in Figure 4c,d. When cycling started, the impedance of the cell with the Mg foil anode dropped to around 500 Ω, which was, however, still much larger
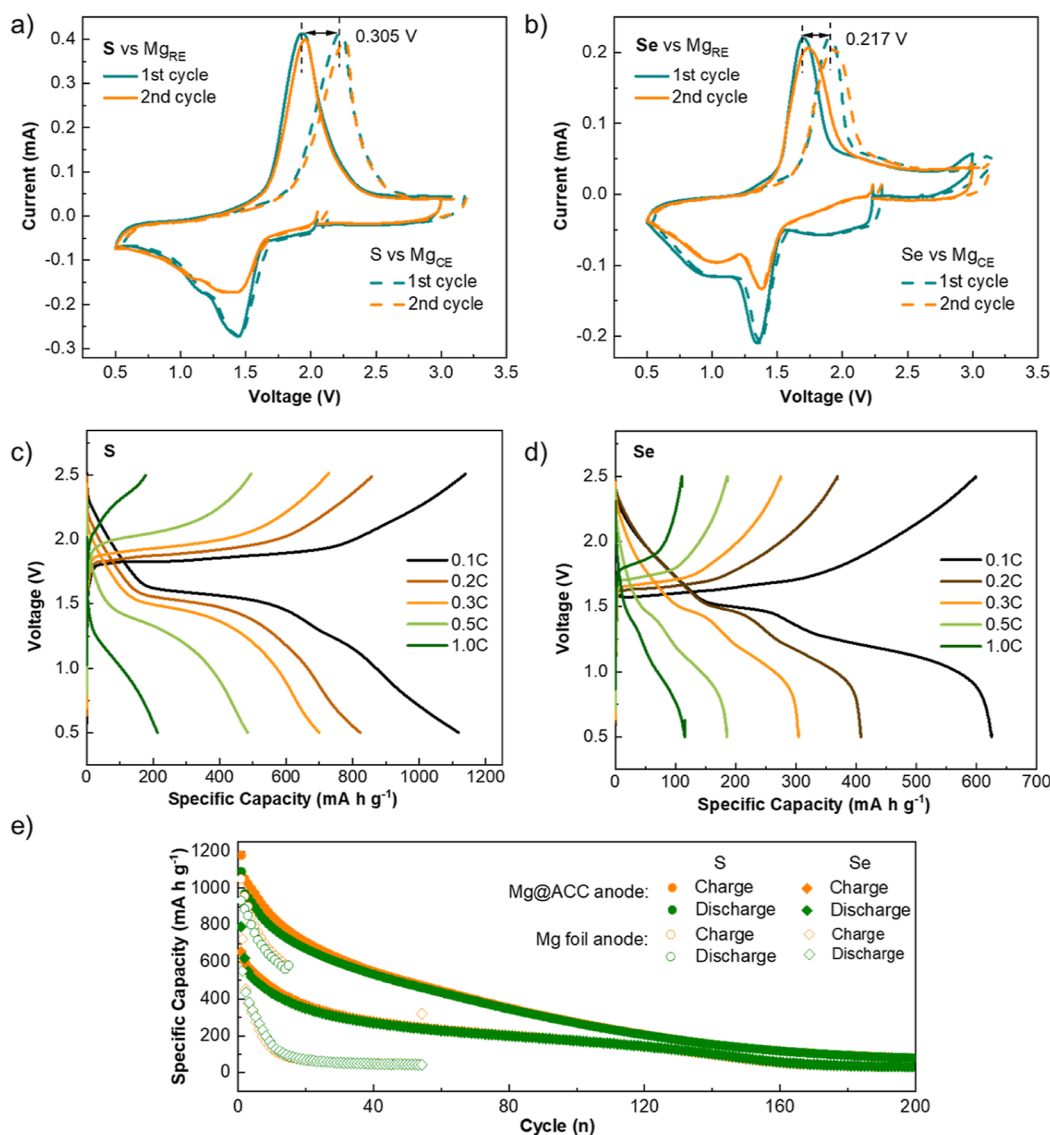
Figure 6. Cyclic voltammetry curves of (a) S|Mg@ACC and (b) Se|Mg@ACC cells with a three-electrode setup for the first two cycles. The scan rate was 0.1 mV s^{-1}. Rate performance of (c) S|Mg@ACC and (d) Se|Mg@ACC cells at current densities of 0.1, 0.2, 0.3, 0.5, and 1 C. (e) Long cycling performance of S|Mg@ACC or Mg foil and Se|Mg@ACC or Mg foil cells at a current density of 0.1 C.

than the cell with the Mg@ACC anode at 300 Ω (Figure S16b). The low impedance of the cell with the Mg@ACC anode is associated with fast charge transfer and enhanced kinetics due to its 3D structure. As illustrated in Figure 5e,f, the interconnected carbon matrix in the Mg@ACC anode can provide extended electrochemically active sites with less insulating passivation by PSs, compared with the Mg foil anode.

The cycling stability and rate capability of cells with the Mg@ ACC anode were further investigated by extending the chalcogen cathode material to selenium. Similar to sulfur, the selenium cathodes were also prepared by a melt-diffusion method and characterized with SEM−EDX, as shown in Figure S17. Cyclic voltammetry curves of cells with S or Se cathodes versus Mg@ACC anodes in a three-electrode setup are presented in Figure 6a,b. For both Mg−S and Mg−Se cells, the main reduction peak overlapped with respect to the reference electrode and counter electrode during the first two cathodic scans, indicating negligible overpotentials during the Mg stripping process with Mg@ACC. During the cathode oxidation, the potential differences were small, 0.305 V for the

Mg−S and 0.217 V for the Mg−Se cell, which are attributed to the fast charge transfer of the anode as discussed before. The enhanced kinetics were further validated by the rate performances of the Mg−S and Mg−Se cells (Figure 6c,d). The cycling performances of the Mg−S and Mg−Se cells with different anodes (Mg@ACC and Mg foil) were evaluated at 0.1 C (Figure 6e). Moreover, the long-term cycling performances of both Mg−S and Mg−Se cells are shown in Figure S18, up to 800 cycles without an anode failure. However, capacity fading still exists due to the infamous shuttle effect.[24] Besides, ACC was reported with a good polysulfide absorption capability,[55] which may cause the irreversible loss of the active material with some exposure of the carbon fiber surface after long cycling. The excellent rate and cycle life of the cells demonstrates that the 3D conductive carbon framework is beneficial for accelerating charge transfer and homogenizing the metal deposits. Moreover, with its enlarged specific surface area and special structure, it guarantees sufficient numbers of electrochemically active sites, thus avoiding the detrimental passivation of the Mg anode in Mg−S or Mg−Se cells, as illustrated in Figure 5e,f. Finally,

postmortem SEM images of Mg@ACC after cycling are shown in Figure S19. In brief, the morphology and structure of the plated Mg layer were maintained, indicating the good stability and reversibility of the electrode.

3. CONCLUSIONS

In summary, the anode failure mechanism of the Mg–chalcogen battery was investigated, which is highly related to the inhomogeneous nucleation and growth of Mg on the anode surface. During the charge process, there is a competition between sulfur species reduction and Mg^{2+} reduction (or Mg plating) on the anode. The freshly nonuniformly plated Mg reacts continuously with dissolved polysulfides a nd produces "dead Mg," which leads to cell failure. Therefore, a special Mg anode with a 3 D functional host was designed and further confirmed this conclusion. The soft carbon matrix can regulate a uniform Mg electrodeposition with a reduced nucleation barrier, leading to a much reduced initial overpotential of −0.16 V. In Mg–S/Mg–Se batteries, superior cycle life (up to 800 cycles) and low resistance upon cycling are obtained. This work provides insights into the failure mechanism of magnesium metal anodes and offers an effective pathway of anode structural design toward great breakthroughs in Mg–based batteries.

4. EXPERIMENTAL SECTION

4.1. Electrolyte Synthesis. Commercially available anhydrous dimethoxy ethane (DME, Sigma) was stored over 3 Å molecular sieves in a glove box for at least 24 h prior to use. Hexafluoroisopropanol $((CF_3)_2CHOH$, 99%, Alfa Aesar) was dried over 3 and 4 Å mixed molecular sieves. $NaBH_4$ (98%, Sigma-Aldrich) and anhydrous $MgCl_2$ (99%, Sigma-Aldrich) were used as received to produce $Mg(BH_4)_2$. The magnesium tetrakis(hexafluoroisopropyloxy)borate $(Mg[B-(hfip)_4]_2)$ electrolyte was synthesized in a reaction between $Mg(BH_4)_2$ and hexafluoroisopropanol in DME as reported.[40] The 0.4 M electrolyte solution was prepared by dissolving a proper amount of magnesium salt in DME; the concentration was based on the molecular weight of $Mg[B(hfip)_4]_2 \cdot 3DME$.

4.2. Preparation of the Mg@ACC Anode. A galvanostatic electrodeposition method was used to prepare Mg@ACC anodes, as shown in Figure 2a. Before electrodeposition, the activated carbon cloth (ACC-507-20, Kynol Europa GmbH) and glass fiber membranes [(GF/C) from Whatman] were tailored into proper discs with a diameter of 13 or 16 mm and vacuum dried at 230 °C overnight. CR2032-type coin cells were assembled to deposit magnesium on ACC. The coin cells were composed of a magnesium foil as the counter/reference electrode, a porous glass fiber separator, and a piece of ACC as the working electrode. The cells were operated with an Arbin battery cycling unit at a discharge current density of 1 mA cm^{-2} at 25 °C. The electrodeposition stabilized at around 0.25 V versus Mg^{2+}/Mg in the electrolyte containing 0.4 M $Mg[B(hfip)_4]_2 \cdot 3DME$ and was stopped after 4 h.

4.3. Preparation of Magnesium Polysulfide Solution. 2.053 g (64.0 mmol) of sulfur powder and 0.194 g (8.0 mmol) of Mg crumbs scratched from Mg foil were added to a glass vial and mixed with 30 mL of tetraglyme in a glove box. The suspension was then stirred at 60 °C for 3 days. Finally, the suspension was filtered, and the reddish polysulfide solution (shown in Figure S13) was used for symmetric cell testing.

4.4. Preparation of ACC/S and ACC/Se Cathodes and the Mg Anode. The preparation of the ACC/S composite follows previously published protocols.[10,56] The ACC was first punched into circular discs with a diameter of 10 mm and dried under vacuum at 230 °C overnight. Elemental sulfur (99.98%, Sigma-Aldrich) was homogeneously dispersed on the ACC discs. The obtained discs were transferred into a glass tube with a diameter of 1 cm. The glass tube was then sealed under vacuum and heated to 160 °C for 16 h. Sulfur loading was determined by subtracting the mass of blank ACC from the loaded

ACC. This amount corresponded to a sulfur loading of 0.7−0.9 mg cm^{-2}. Similarly, for the ACC/Se composite, instead of sulfur, elemental selenium (99.98%, Sigma-Aldrich) was used at a higher temperature of 260 °C. The selenium loading was around 0.7−0.9 mg cm^{-2}.

In comparison, magnesium foil (0.1 mm, Gelon Energy Corp) was also used as an anode. Prior to cell assembly, Mg discs were tailored into proper discs with a diameter of 13 mm and scratched carefully on both sides in the glovebox to remove the native oxide layer from their surface.

4.5. Characterization. XRD measurements were conducted on a STOE STADI diffractometer with a Mo Kα X-ray source operated at 50 kV and 40 mA in the range of 10−40°. SEM images were obtained using a ZEISS LEO 1530 at 10 kV electron beam with EDX. The SEM samples were prepared on carbon tapes. The chemical state of the surface of the separator(s) was determined by XPS measurements using a Specs XPS system with a Phoibos 150 energy analyzer. The spectra were recorded with monochromatized Al Kα radiation (400 W, 15 kV) at a detection angle of 45° with pass energies of 90 and 30 eV for the survey and detail measurements, respectively. For binding energy calibration, the main C 1s peak of adventitious carbon was set to 284.8 eV. Peak fitting was done with CasaXPS using Shirly-type backgrounds and Gaussian−Lorentzian peak profiles.

4.6. Electrochemical Measurements. The CR2032 coin cells and three-electrode cells (PAT-Cell, EL-CELL) were assembled in an argon−filled glove box (H_2O, O_2 < 0.1 ppm). The glass fiber (GF, Whatman, GF/C) membranes were vacuum dried at 230 °C overnight and were as a separator. Symmetric and asymmetric cells were employed to evaluate the cycling stability and cycle lifespan of the anodes. During the electrochemical process, magnesium was continuously plated or stripped at a current density of 0.1 mA cm^{-2}. Electrochemical impedance spectroscopy (EIS) was carried out on an electrochemical workstation (VMP-3 Biologic) from 1 MHz to 20 mHz with a DC voltage amplitude of 10 mV. For Mg−S/Mg−Se coin cells, galvanostatic charge/discharge experiments were performed in a voltage range of 0.5−2.5 V versus Mg/Mg^{2+} and at a current density of 0.1 C (S: 1 C = 1675 mA g^{-1}; Se: 1 C = 675 mA g^{-1}). Cyclic voltammetry measurements were carried out with a scan rate of 0.1 mV s^{-1} in a voltage range of 0.5−3.0 V versus Mg/Mg^{2+} on a Biologic VMP-3 potentiostat. All electrochemical investigations were conducted at 25 °C.

AUTHOR INFORMATION

Corresponding Authors

Liping Wang − *Helmholtz Institute Ulm (HIU) Electrochemical Energy Storage, Ulm D-89081, Germany;* orcid.org/0000-0002-4113-2208; Email: liping.wang@partner.kit.edu

Zhirong Zhao-Karger − *Helmholtz Institute Ulm (HIU) Electrochemical Energy Storage, Ulm D-89081, Germany; Institute of Nanotechnology (INT), Karlsruhe Institute of Technology (KIT), Hermann-von-Helmholtz-Platz 1, Eggenstein-Leopoldshafen D-76344, Germany;* orcid.org/0000-0002-7233-9818; Email: zhirong.zhao-karger@kit.edu

Authors

Thomas Diemant − *Helmholtz Institute Ulm (HIU) Electrochemical Energy Storage, Ulm D-89081, Germany*

Zhenyou Li − *Helmholtz Institute Ulm (HIU) Electrochemical Energy Storage, Ulm D-89081, Germany;* ⓞ orcid.org/0000-0001-9624-2124

Bosubabu Dasari − *Helmholtz Institute Ulm (HIU) Electrochemical Energy Storage, Ulm D-89081, Germany;* ⓞ orcid.org/0000-0001-8816-2984

Notes

The authors declare no competing financial interest.

ACKNOWLEDGMENTS

REFERENCES

(1) Gregory, T. D.; Hoffman, R. J.; Winterton, R. C. Nonaqueous electrochemistry of magnesium: applications to energy storage. *J. Electrochem. Soc.* **1990**, *137*, 775.

(2) Besenhard, J. O.; Winter, M. Advances in Battery Technology: Rechargeable Magnesium Batteries and Novel Negative-Electrode Materials for Lithium Ion Batteries. *ChemPhysChem* **2002**, *3*, 155−159.

(3) Yoo, H. D.; Shterenberg, I.; Gofer, Y.; Gershinsky, G.; Pour, N.; Aurbach, D. Mg rechargeable batteries: an on-going challenge. *Energy Environ. Sci.* **2013**, *6*, 2265−2279.

(4) Mohtadi, R.; Mizuno, F. Magnesium batteries: Current state of the art, issues and future perspectives. *Beilstein J. Nanotechnol.* **2014**, *5*, 1291−1311.

(5) Deivanayagam, R.; Ingram, B. J.; Shahbazian-Yassar, R. Progress in development of electrolytes for magnesium batteries. *Energy Storage Mater.* **2019**, *21*, 136−153.

(6) Mohtadi, R.; Tutusaus, O.; Arthur, T. S.; Zhao-Karger, Z.; Fichtner, M. The metamorphosis of rechargeable magnesium batteries. *Joule* **2021**, *5*, 581−617.

(7) Park, B.; Schaefer, J. L. Review-Polymer Electrolytes for Magnesium Batteries: Forging Away from Analogs of Lithium Polymer Electrolytes and Towards the Rechargeable Magnesium Metal Polymer Battery. *J. Electrochem. Soc.* **2020**, *167*, 070545.

(8) Wang, P. W.; Buchmeiser, M. R. Rechargeable Magnesium-Sulfur Battery Technology: State of the Art and Key Challenges. *Adv. Funct. Mater.* **2019**, *29*, 1905248.

(9) Gao, T.; Noked, M.; Pearse, A. J.; Gillette, E.; Fan, X.; Zhu, Y.; Luo, C.; Suo, L.; Schroeder, M. A.; Xu, K.; Lee, S. B.; Rubloff, G. W.; Wang, C. Enhancing the Reversibility of Mg/S Battery Chemistry through Li$^+$ Mediation. *J. Am. Chem. Soc.* **2015**, *137*, 12388−12393.

(10) Meng, Z.; Foix, D.; Brun, N.; Dedryvère, R.; Stievano, L.; Morcrette, M.; Berthelot, R. Alloys to Replace Mg Anodes in Efficient and Practical Mg-Ion/Sulfur Batteries. *ACS Energy Lett.* **2019**, *4*, 2040−2044.

(11) Li, Z.; Mu, X.; Zhao-Karger, Z.; Diemant, T.; Behm, R. J.; Kübel, C.; Fichtner, M. Fast kinetics of multivalent intercalation chemistry enabled by solvated magnesium-ions into self-established metallic layered materials. *Nat. Commun.* **2018**, *9*, 5115.

(12) Muldoon, J.; Bucur, C. B.; Gregory, T. Quest for Nonaqueous Multivalent Secondary Batteries: Magnesium and Beyond. *Chem. Rev.* **2014**, *114*, 11683−11720.

(13) Wu, Z.; Curtin, W. A. The origins of high hardening and low ductility in magnesium. *Nature* **2015**, *526*, 62−67.

(14) Schloffer, D.; Bozorgi, S.; Sherstnev, P.; Lenardt, C.; Gollas, B. Manufacturing and characterization of magnesium alloy foils for use as anode materials in rechargeable magnesium ion batteries. *J. Power Sources* **2017**, *367*, 138−144.

(15) Tutusaus, O.; Mohtadi, R.; Singh, N.; Arthur, T. S.; Mizuno, F. Study of Electrochemical Phenomena Observed at the Mg Metal/Electrolyte Interface. *ACS Energy Lett.* **2017**, *2*, 224−229.

(16) Connell, J. G.; Genorio, B.; Lopes, P. P.; Strmcnik, D.; Stamenkovic, V. R.; Markovic, N. M. Tuning the Reversibility of Mg Anodes via Controlled Surface Passivation by H2O/Cl− in Organic Electrolytes. *Chem. Mater.* **2016**, *28*, 8268−8277.

(17) Cheng, X.-B.; Zhang, R.; Zhao, C.-Z.; Zhang, Q. Toward Safe Lithium Metal Anode in Rechargeable Batteries: A Review. *Chem. Rev.* **2017**, *117*, 10403−10473.

(18) Li, D.; Yuan, Y.; Liu, J.; Fichtner, M.; Pan, F. A review on current anode materials for rechargeable Mg batteries. *J. Magnesium Alloys* **2020**, *8*, 963−979.

(19) Aurbach, D.; Gizbar, H.; Schechter, A.; Chusid, O.; Gottlieb, H. E.; Gofer, Y.; Goldberg, I. Electrolyte Solutions for Rechargeable Magnesium Batteries Based on Organomagnesium Chloroaluminate Complexes. *J. Electrochem. Soc.* **2001**, *149*, A115−A121.

(20) Lu, Z.; Schechter, A.; Moshkovich, M.; Aurbach, D. On the electrochemical behavior of magnesium electrodes in polar aprotic electrolyte solutions. *J. Electroanal. Chem.* **1999**, *466*, 203−217.

(21) Bieker, G.; Küpers, V.; Kolek, M.; Winter, M. Intrinsic differences and realistic perspectives of lithium-sulfur and magnesium-sulfur batteries. *Commun. Mater.* **2021**, *2*, 37.

(22) Jayasyaee, K.; Rerthelot, R.; Lethesh, K. C.; Sheridan, E. M. Anode materials for rechargeable Mg batteries. *Magnesium Batteries*; Royal Society of Chemistry, 2019; pp 114−141.

(23) Richter, R.; Häcker, J.; Zhao-Karger, Z.; Danner, T.; Wagner, N.; Fichtner, M.; Friedrich, K. A.; Latz, A. Insights into Self-Discharge of Lithium− and Magnesium−Sulfur Batteries. *ACS Appl. Energy Mater.* **2020**, *3*, 8457−8474.

(24) Ford, H. O.; Doyle, E. S.; He, P.; Boggess, W. C.; Oliver, A. G.; Wu, T.; Sterbinsky, G. E.; Schaefer, J. L. Self-discharge of magnesium−sulfur batteries leads to active material loss and poor shelf life. *Energy Environ. Sci.* **2021**, *14*, 890−899.

(25) Richter, R.; Häcker, J.; Zhao-Karger, Z.; Danner, T.; Wagner, N.; Fichtner, M.; Friedrich, K. A.; Latz, A. Degradation Effects in Metal−Sulfur Batteries. *ACS Appl. Energy Mater.* **2021**, *4*, 2365−2376.

(26) Gao, T.; Hou, S.; Huynh, K.; Wang, F.; Eidson, N.; Fan, X.; Han, F.; Luo, C.; Mao, M.; Li, X.; Wang, C. Existence of Solid Electrolyte Interphase in Mg Batteries: Mg/S Chemistry as an Example. *ACS Appl. Mater. Interfaces* **2018**, *10*, 14767−14776.

(27) Zhao-Karger, Z.; Lin, X.-M.; Bonatto Minella, C.; Wang, D.; Diemant, T.; Behm, R. J.; Fichtner, M. Selenium and selenium-sulfur cathode materials for high-energy rechargeable magnesium batteries. *J. Power Sources* **2016**, *323*, 213−219.

(28) Salama, M.; Attias, R.; Hirsch, B.; Yemini, R.; Gofer, Y.; Noked, M.; Aurbach, D. On the Feasibility of Practical Mg-S Batteries: Practical Limitations Associated with Metallic Magnesium Anodes. *ACS Appl. Mater. Interfaces* **2018**, *10*, 36910−36917.

(29) Nguyen, D.-T.; Horia, R.; Eng, A. Y. S.; Song, S.-W.; Seh, Z. W. Material design strategies to improve the performance of rechargeable magnesium−sulfur batteries. *Mater. Horiz.* **2021**, *8*, 830−853.

(30) Ren, W.; Wu, D.; NuLi, Y.; Zhang, X.; Yang, J.; Wang, J. A Chlorine-Free Electrolyte Based on Non-nucleophilic Magnesium Bis(diisopropyl)amide and Ionic Liquid for Rechargeable Magnesium Batteries. *ACS Appl. Mater. Interfaces* **2021**, *13*, 32957−32967.

(31) Li, Y.; Zheng, Y.; Guo, K.; Zhao, J.; Li, C. Mg-Li Hybrid Batteries: The Combination of Fast Kinetics and Reduced Overpotential. *Energy Mater. Adv.* **2022**, *2022*, 9840837.

(32) Li, Y.; Zhou, X.; Hu, J.; Zheng, Y.; Huang, M.; Guo, K.; Li, C. Reversible Mg metal anode in conventional electrolyte enabled by durable heterogeneous SEI with low surface diffusion barrier. *Energy Storage Mater.* **2022**, *46*, 1−9.

(33) Zhou, X.; Tian, J.; Hu, J.; Li, C. High Rate Magnesium−Sulfur Battery with Improved Cyclability Based on Metal−Organic Framework Derivative Carbon Host. *Adv. Mater.* **2018**, *30*, 1704166.

(34) Vinayan, B. P.; Euchner, H.; Zhao-Karger, Z.; Cambaz, M. A.; Li, Z.; Diemant, T.; Behm, R. J.; Gross, A.; Fichtner, M. Insights into the electrochemical processes of rechargeable magnesium−sulfur batteries with a new cathode design. *J. Mater. Chem. A* **2019**, *7*, 25490−25502.

(35) Wang, L.; Jankowski, P.; Njel, C.; Bauer, W.; Li, Z.; Meng, Z.; Dasari, B.; Vegge, T.; Lastra, J. M. G.; Zhao-Karger, Z.; Fichtner, M. Dual Role of Mo6 S8 in Polysulfide Conversion and Shuttle for Mg-S Batteries. *Adv. Sci.* **2022**, *9*, 2104605.

(36) Ji, Y. C.; Liu-Théato, X.; Xiu, Y. L.; Indris, S.; Njel, C.; Maibach, J.; Ehrenberg, H.; Fichtner, M.; Zhao-Karger, Z. Polyoxometalate Modified Separator for Performance Enhancement of Magnesium-Sulfur Batteries. *Adv. Funct. Mater.* **2021**, *31*, 2100868.

(37) Sievert, B.; Häcker, J.; Bienen, F.; Wagner, N.; Friedrich, K. A. Magnesium Sulfur Battery with a New Magnesium Powder Anode. *ECS Trans.* **2017**, *77*, 413−424.

(38) Bevilacqua, S. C.; Pham, K. H.; See, K. A. Effect of the Electrolyte Solvent on Redox Processes in Mg−S Batteries. *Inorg. Chem.* **2019**, *58*, 10472−10482.

(39) Li, X.; Gao, T.; Han, F.; Ma, Z.; Fan, X.; Hou, S.; Eidson, N.; Li, W.; Wang, C. Reducing Mg Anode Overpotential via Ion Conductive Surface Layer Formation by Iodine Additive. *Adv. Energy Mater.* **2018**, *8*, 1701728.

(40) Zhao-Karger, Z.; Liu, R.; Dai, W.; Li, Z.; Diemant, T.; Vinayan, B. P.; Bonatto Minella, C.; Yu, X.; Manthiram, A.; Behm, R. J.; Ruben, M.; Fichtner, M. Toward Highly Reversible Magnesium−Sulfur Batteries with Efficient and Practical Mg[B(hfip)$_4$]$_2$Electrolyte. *ACS Energy Lett.* **2018**, *3*, 2005−2013.

(41) Yu, X.; Manthiram, A. Performance Enhancement and Mechanistic Studies of Magnesium−Sulfur Cells with an Advanced Cathode Structure. *ACS Energy Lett.* **2016**, *1*, 431−437.

(42) Song, Z.; Zhang, Z.; Du, A.; Dong, S.; Li, G.; Cui, G. Uniform Magnesium Electrodeposition via Synergistic Coupling of Current Homogenization, Geometric Confinement, and Chemisorption Effect. *Adv. Mater.* **2021**, *33*, 2100224.

(43) Wang, J.; Zhao, W.; Dou, H.; Wan, B.; Zhang, Y.; Li, W.; Zhao, X.; Yang, X. Electrostatic Shielding Guides Lateral Deposition for Stable Interphase toward Reversible Magnesium Metal Anodes. *ACS Appl. Mater. Interfaces* **2020**, *12*, 19601−19606.

(44) Ding, M. S.; Diemant, T.; Behm, R. J.; Passerini, S.; Giffin, G. A. Dendrite Growth in Mg Metal Cells Containing Mg(TFSI)2/Glyme Electrolytes. *J. Electrochem. Soc.* **2018**, *165*, A1983−A1990.

(45) Davidson, R.; Verma, A.; Santos, D.; Hao, F.; Fincher, C.; Xiang, S.; Van Buskirk, J.; Xie, K.; Pharr, M.; Mukherjee, P. P.; Banerjee, S. Formation of Magnesium Dendrites during Electrodeposition. *ACS Energy Lett.* **2019**, *4*, 375−376.

(46) Kwak, J. H.; Jeoun, Y.; Oh, S. H.; Yu, S.; Lim, J.-H.; Sung, Y.-E.; Yu, S.-H.; Lim, H.-D. Operando Visualization of Morphological Evolution in Mg Metal Anode: Insight into Dendrite Suppression for Stable Mg Metal Batteries. *ACS Energy Lett.* **2022**, *7*, 162−170.

(47) Richter, R.; Häcker, J.; Zhao-Karger, Z.; Danner, T.; Wagner, N.; Fichtner, M.; Friedrich, K. A.; Latz, A. Insights into Self-Discharge of Lithium− and Magnesium−Sulfur Batteries. *ACS Appl. Energy Mater.* **2020**, *3*, 8457−8474.

(48) Meng, J.; Chu, F.; Hu, J.; Li, C. Liquid Polydimethylsiloxane Grafting to Enable Dendrite-Free Li Plating for Highly Reversible Li-Metal Batteries. *Adv. Funct. Mater.* **2019**, *29*, 1902220.

(49) Hu, J.; Chen, K.; Li, C. Nanostructured Li-Rich Fluoride Coated by Ionic Liquid as High Ion-Conductivity Solid Electrolyte Additive to Suppress Dendrite Growth at Li Metal Anode. *ACS Appl. Mater. Interfaces* **2018**, *10*, 34322−34331.

(50) Chu, F.; Hu, J.; Tian, J.; Zhou, X.; Li, Z.; Li, C. In Situ Plating of Porous Mg Network Layer to Reinforce Anode Dendrite Suppression in Li-Metal Batteries. *ACS Appl. Mater. Interfaces* **2018**, *10*, 12678−12689.

(51) Hu, J.; Tian, J.; Li, C. Nanostructured Carbon Nitride Polymer-Reinforced Electrolyte To Enable Dendrite-Suppressed Lithium Metal Batteries. *ACS Appl. Mater. Interfaces* **2017**, *9*, 11615−11625.

(52) Zuo, T.-T.; Wu, X.-W.; Yang, C.-P.; Yin, Y.-X.; Ye, H.; Li, N.-W.; Guo, Y.-G. Graphitized Carbon Fibers as Multifunctional 3D Current Collectors for High Areal Capacity Li Anodes. *Adv. Mater.* **2017**, *29*, 1700389.

(53) Huang, G.; Han, J.; Zhang, F.; Wang, Z.; Kashani, H.; Watanabe, K.; Chen, M. Lithiophilic 3D Nanoporous Nitrogen-Doped Graphene for Dendrite-Free and Ultrahigh-Rate Lithium-Metal Anodes. *Adv. Mater.* **2019**, *31*, 1805334.

(54) Laskowski, F. A. L.; Stradley, S. H.; Qian, M. D.; See, K. A. Mg Anode Passivation Caused by the Reaction of Dissolved Sulfur in Mg−S Batteries. *ACS Appl. Mater. Interfaces* **2021**, *13*, 29461−29470.

(55) Bosubabu, D.; Li, Z.; Meng, Z.; Wang, L.-P.; Fichtner, M.; Zhao-Karger, Z. Mitigating self-discharge and improving the performance of Mg−S battery in Mg[B(hfip)$_4$]$_2$ electrolyte with a protective interlayer. *J. Mater. Chem. A* **2021**, *9*, 25150−25159.

(56) Gao, T.; Hou, S.; Wang, F.; Ma, Z.; Li, X.; Xu, K.; Wang, C. Reversible S^0/MgS$_x$ Redox Chemistry in a MgTFSI$_2$/MgCl$_2$/DME Electrolyte for Rechargeable Mg/S Batteries. *Angew. Chem., Int. Ed.* **2017**, *56*, 13526−13530.